THE JOURNAL OF PHYSICAL CHEMISTRY C

Article

pubs.acs.org/JPCC

# Role of Graphene Oxide as a Sacrificial Interlayer for Enhanced Photoelectrochemical Water Oxidation of Hematite Nanorods

Alagappan Annamalai,[†] Aravindaraj G. Kannan,[‡] Su Yong Lee,[§] Dong-Won Kim,[‡] Sun Hee Choi,[*,§] and Jum Suk Jang[*,†]

[†]Division of Biotechnology Advanced Institute of Environmental and Bioscience, College of Environmental and Bioresource Sciences, Chonbuk National University, Iksan 570-752, Korea

[‡]Department of Chemical Engineering, Hanyang University, Seoul 133-791, Korea

[§]Pohang Accelerator Laboratory, POSTECH, Pohang 790-784, Korea

*Supporting Information*

**ABSTRACT:** Photoelectrochemical cells (PECs) with a structure of F-doped $SnO_2$ (FTO)/graphene oxide (GO)/hematite ($\alpha$-$Fe_2O_3$) photoanode were fabricated, in which GO serves as a sacrificial underlayer. In contrast to low-temperature sintering carried out under a normal atmosphere, high-temperature sintering was carried out for the GO underlayer-based hematite photoanodes. The photocurrent density of the PECs with GO underlayers gradually increased as the spin speed of the FTO substrate increased. In particular, GO at a spin speed of 5000 rpm showed the highest photocurrent of 1.3 mA/cm$^2$. The higher performance of the GO/$\alpha$-$Fe_2O_3$ photoanodes was attributed to the improved FTO/$\alpha$-$Fe_2O_3$ interface. When sintered at 800 °C for activation of the hematite (FTO/GO/$\alpha$-$Fe_2O_3$) photoanodes, the GO layers before being decomposed act as localized hot zones at the FTO/$\alpha$-$Fe_2O_3$ interface. These localized hot zones play a very crucial role in reducing the microstrain (increased crystallinity) which was confirmed from the synchrotron X-ray diffraction studies. The sacrificial GO underlayer may contribute to relaxing the inhomogeneous internal strain of the $\alpha$-$Fe_2O_3$ nanorods and reducing the deformation of FTO to an extent. In other words, the reduction of the microstrain minimizes the lattice imperfections and defects at the FTO/$\alpha$-$Fe_2O_3$ interface, which may enhance the charge collection efficiency, as demonstrated by the impedance measurements. From the EXAFS analysis, it is clearly evident that the sacrificial GO underlayer does not affect the structure of $\alpha$-$Fe_2O_3$ in the short range. The effects of the GO sacrificial layers are restricted to the FTO/$\alpha$-$Fe_2O_3$ interface, and they do not affect the bulk properties of $\alpha$-$Fe_2O_3$.

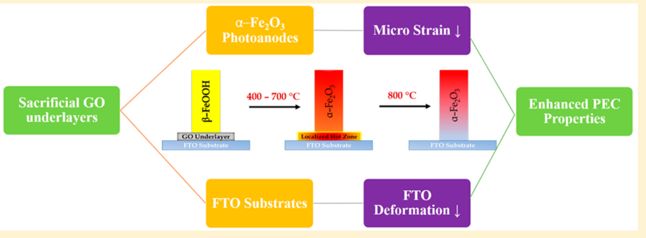


## INTRODUCTION

Hematite ($\alpha$-$Fe_2O_3$) is a promising photoanode material for solar water splitting which is abundant, nontoxic, chemically stable, and low cost and has an optimum bandgap of ~2.2 eV.[1−4] The above properties make $\alpha$-$Fe_2O_3$ the most studied metal-oxide semiconductor photoanode for photoelectrochemical cell (PEC) water splitting. Charge recombination is a major issue in PECs which limits the device performance.[5] Transparent conducting oxide (TCO)/photoanode interfaces are highly prone to charge recombination.[6] The charge transport resistance of the TCO/photoanode interface plays an important role in the charge collection efficiency and, consequently, in the overall device performance.[7] The charge collection efficiency is simply the ratio of the short-circuit current and the total light-generated current. The charge collection depends on two main factors, namely, recombination and diffusion.[8] When there is a better electron pathway (1-D nanostructures), the TCO/photoanode interface plays a crucial role in the determination of charge collection.[9] Recently, great effort has been devoted toward the introduction of a metal oxide semiconductor as the underlayer at the interface of the $SnO_2$:F (FTO) substrate and $\alpha$-$Fe_2O_3$ photoanodes.[10] Metal oxide underlayers such as $SiO_2$,[7,11] $TiO_2$,[7,12] $Ga_2O_3$,[13] and $Nb_2O_5$[7] enhance the photoactivity of hematite photoanodes. The metal oxide underlayer physically blocks the recombination of the photoinjected electrons at the FTO/$\alpha$-$Fe_2O_3$ interface.[14] Recently, we demonstrated $TiO_2$ underlayers for water splitting with enhancement of the photocurrent at both 550 and 800 °C, as the $TiO_2$ underlayer acts as a recombination barrier and also as a source for $Ti^{4+}$ dopants.[12] Graphene-based photoanodes are widely used in photovoltaics, organic light-emitting diodes, and PEC cells[15] due to their higher electron mobility, transparency, and flexibility.[16,17] Zhang et al.[18] reported that a graphene interlayer inserted into inverse opal $\alpha$-$Fe_2O_3$ photoanodes enhanced the photoactivity by reducing the charge recombination and, at the same time, acts as an electron transport layer. Sintering conditions have been carefully controlled such that the deposited $Fe^0$ is successfully

**Received:** July 5, 2015
**Revised:** August 9, 2015
**Published:** August 10, 2015

Scheme 1. Effect of Sacrificial GO Underlayers on Hematite Photoanodes Subjected to High-Temperature Sintering

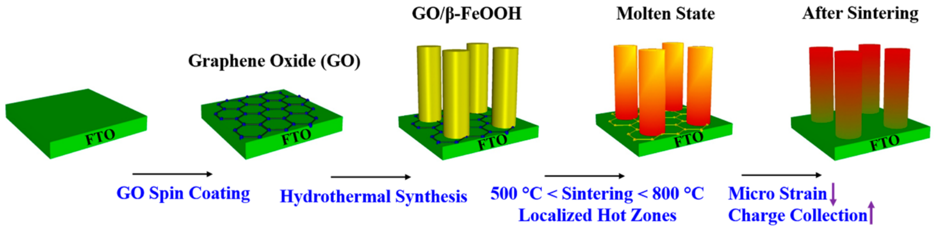


converted into $\alpha$-$Fe_2O_3$ without damaging graphene underlayers as graphene is not stable above 525 °C.[18] However, a high sintering temperature (~800 °C) is required for the activation of hematite photoanodes.[19] Most graphene-based underlayer/interlayer photoanodes are sintered either at a low temperature or at a high temperature under an inert atmosphere in order to preserve the graphene-based underlayer in the final device.[20] It is widely known that GO-based materials are not stable at 800 °C under normal atmospheric conditions due to the thermal oxidation of carbon compounds into $CO_2$.[18] Yoon et al. reported a two-step sintering process at 350 °C for 4 h and 750 °C for 1 h under an Ar atmosphere in order to preserve the graphene-based underlayer in the final device after activation. The performance of such devices is found to be dependent on the sintering temperature and atmosphere. However, such devices have not been sintered at high temperature in oxidizing conditions, where thermal oxidation of GO can act as a "heat zone" and could influence the crystallinity of the oxides, thereby influencing the interfacial behavior. Hence, we explored sintering FTO/GO/$\alpha$-$Fe_2O_3$ photoanodes at 800 °C in oxygen atmosphere (Scheme 1), and to our surprise, we found that sintering at such conditions enhanced the device performance by 30%. This performance enhancement could be explained based on the changes in the microcrystallinity[21,22] of $\alpha$-$Fe_2O_3$ in the interface as observed by synchrotron XRD measurements. This phenomenon opens the possibility of using GO as a sacrificial layer in devices that require high-temperature sintering in oxidative atmospheres.

Herein we report that the GO underlayers enhance the solar water splitting performance of $\alpha$-$Fe_2O_3$ photoanodes even though the GO underlayer disappeared (sacrificial layer) due to thermal oxidation when sintered at a high temperature (800 °C). This performance enhancement was mainly due to improved interfacial properties (FTO/$\alpha$-$Fe_2O_3$) due to the presence of a sacrificial GO underlayer. During the thermal oxidation of GO sacrificial underlayers, the GO layers act as localized hot zones at the FTO/GO/$\alpha$-$Fe_2O_3$ interface, which minimizes the lattice imperfections (reducing the microstrain) of $\alpha$-$Fe_2O_3$ nanorods and deformation of FTO substrates (charge transfer resistance across the interface between FTO/$\alpha$-$Fe_2O_3$), as confirmed from the synchrotron X-ray studies and impedance measurements, respectively. To the best of our knowledge, this is the first report of sacrificial GO underlayers playing a dual role of enhancing the charge collection efficiency and lowering the microstrain at the FTO/$\alpha$-$Fe_2O_3$ interface, leading to an enhanced photocurrent density.

## ■ EXPERIMENTAL SECTION

Graphite oxide was synthesized from graphite powder (SP-1, 30 μm nominal particle size, Bay Carbon, Bay City, MI) by a modified Hummers method,[23] in which preoxidation of graphite was followed by an oxidation step[24] using the Hummers method. Graphite oxide prepared using the modified Hummers method,[25] was exfoliated in ethanol using sonication to form graphene oxide (GO), and GO (30 mg of GO dispersed in 15 mL of ethanol) was coated onto the FTO substrates by spin coating at various spin speeds (3000−6000 rpm). Hematite nanorods on FTO- and GO-modified FTO substrates were prepared by a simple hydrothermal method as reported by Vayssieres et al.[26] High-temperature sintering (800 °C for 10 min) is carried out, which is believed to be important for activation of the hematite photoanodes.[27] X-ray diffraction (XRD) patterns of all the samples were collected using an X-ray diffactometer (Rigaku RINT 2500) with Cu K$\alpha$ radiation. The effect of the GO underlayer on the crystallinity and strain variation of both the hematite nanostructures and FTO film substrate was investigated by high-resolution X-ray diffraction measurement. X-ray asborption fine structure (XAFS) experiments were carried out on the 7D beamline of Pohang Accelerator Laboratory (PLS-II, 3.0GeV). The synchrotron radiation was monochromatized using a Si(111) double-crystal monochromator. At room temperature, the spectra for the Fe K-edge ($E_0$ = 7112 eV) were taken in a fluorescence mode. The incident beam was detuned by 30% for the Fe K-edge in order to minimize contamination of higher harmonics, and its intensity was monitored using a He-filled IC SPEC ionization chamber. The fluorescence signal from the sample was measured with a passivated implanted planar silicon (PIPS) detector mounted in a He-flowing sample chamber. ATHENA in the IFEFFIT suite of programs was used to analyze the obatined data for the local structure study of Fe in FTO/$\alpha$-$Fe_2O_3$ and FTO/GO/$\alpha$-$Fe_2O_3$.[28] The X-ray wavelength was 1.0716 Å (11.57 keV) for the scattering measurements which were performed at 5A materials science beamline at the Pohang Light Source II (PLS-II) in Korea. The surface morphology of the samples was analyzed using field emission scanning electron microscopy (FESEM, JEOL JSM 700F). Raman spectra were acquired using an excitation energy of 2.4 eV at room temperature. All photoelectrochemical measurements were carried out in 1 M NaOH (pH = 13.8) electrolyte using an Ivium compactstat potentiostat with a platinum coil as counter electrode and Ag/AgCl as reference electrode. Photocurrent−potential ($J$−$V$) curves were swept at 50 mV $s^{-1}$ from −0.7 to +0.7 V vs Ag/AgCl. Impedance spectroscopy measurements were performed using an impedance analyzer (Ivumstat). The impedance spectra were measured over a frequency range of $1 \times 10^{-2}$ to $3 \times 10^{6}$ Hz at 25 °C under open-circuit conditions with amplitude of 10 mV and under a bias illumination of 100 mW $cm^{-2}$.

## ■ RESULTS AND DISCUSSION

To fabricate the FTO/GO/$\alpha$-$Fe_2O_3$ photoanodes, GO was synthesized using the modified Hummers method described elsewhere[25] by spin-coating onto FTO substrates and further


DOI: 10.1021/acs.jpcc.5b06450
J. Phys. Chem. C 2015, 119, 19996−20002

used to synthesize $\alpha$-$Fe_2O_3$ nanorod photoanodes by a hydrothermal method.[19] Figure 1(a) shows the photocurrent density as a function of the applied potential ($I-V$ measurements) of $\alpha$-$Fe_2O_3$ photoanodes with and without a GO underlayer for various spin speeds, demonstrating the importance of controlling the amount of GO present in the interfacial layer. The photocurrent density is enhanced for all of the GO underlayer photoanodes compared to the pristine hematite photoanodes. Varying the spin speed from 3000 to 6000 rpm leads to an improved photocurrent (30% increase) from 1 to 1.3 mA/cm$^2$ at 1.4 V vs RHE, representing a strong dependence on the spin speed (Figure S1). In previous reports,[18,29] the enhancement of device performance with graphene-based underlayers resulted from reduced charge recombination at the FTO/$\alpha$-$Fe_2O_3$ interface. Transient photocurrent measurement of FTO/$\alpha$-$Fe_2O_3$ and FTO/GO/$\alpha$-$Fe_2O_3$ photoanodes as a function of constant applied potential (1.1 V vs RHE) in 1 M NaOH electrolyte is shown in Figure 1(b). At a constant potential (1.1 V), the current decay ($I_d$) (difference between the initial current ($I_i$) and final current ($I_f$); $I_d = I_i - I_f$) decreases from 0.2 to 0.07 mA/cm$^2$ for FTO/GO/$\alpha$-$Fe_2O_3$ photoanodes compared to FTO/$\alpha$-$Fe_2O_3$ photoanodes. Enhanced electron transport results in a suppressed current decay which is in good agreement with the dark current measurements and impedance spectra. We will discuss the critical factors affecting the device performance as a function of the presence of an underlayer.

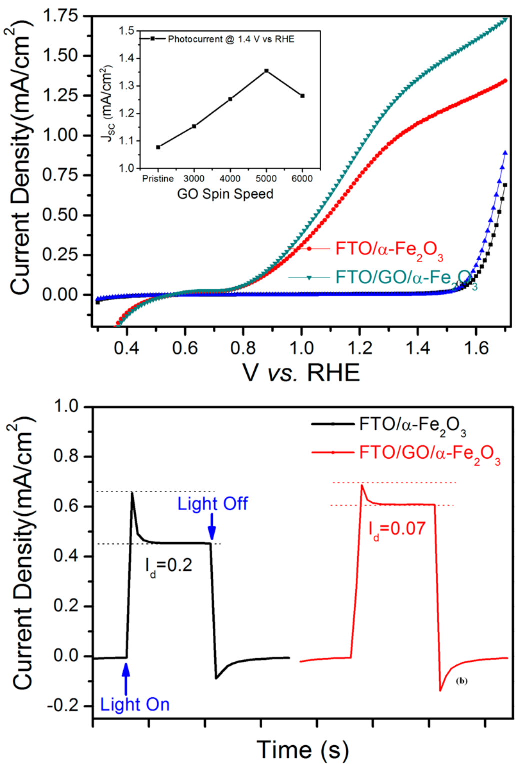


**Figure 1.** (a) Photocurrent−potential ($J-V$) curves and (b) transient photocurrent measurement for the PEC water oxidation reaction with and without GO-based $\alpha$-$Fe_2O_3$ photoanodes in FTO substrates sintered at 800 °C. 1 M NaOH was used under 1 sun standard illumination conditions, and the inset shows the photocurrent densities of the hematite photoanodes with and without GO underlayers at 1.4 V vs RHE under 1 sun standard illumination conditions.

It is very important to understand why GO underlayers enhance the PEC properties of $\alpha$-$Fe_2O_3$ photoanodes after the oxidation process of GO layers at high-temperature sintering. The critical factors responsible for enhanced performance include the following. The effects of GO underlayers on the morphology and crystal growth were characterized first. The structural analysis confirms that there are no obvious changes either in the crystal phase (Figure S2) or in the morphology (Figure 2(a) and (b)) of the $\alpha$-$Fe_2O_3$ photoanodes synthesized with and without a GO underlayer. Although both $\alpha$-$Fe_2O_3$ photoanodes with and without a GO underlayer displayed similar XRD patterns with a predominant (110) diffraction peak (Figure 2(d) and (e)), the photoanodes with a GO underlayer had a relatively narrow peak width. To separate the size and microstrain effects on the peak broadening, a Williamson−Hall plot was developed and is depicted in Figure 2(e).[30,31] Obviously, the photoanode with a GO underlayer has a smaller slope, indicating reduced microstrain on the hematite nanorods. However, a clear peak shift was observed on the FTO substrate with the GO underlayer toward lower scattering angles, as depicted in Figure S3. This angle shift implies that additional compressive strain was applied to the FTO substrate. In the meantime, no peak shift occurred on the $\alpha$-$Fe_2O_3$ photoanodes. The parameters including the crystallite size ($D$), mean microstrain ($\varepsilon$), and $d$-spacing of the hematite (220) and FTO (400) peaks are summarized in Table 1, where the $d$-spacing variation was calculated by $\delta = (d_{GO} - d_{Pris})/d_{Pris}$ in the same manner as the lattice misfit. A decrease of the microstrain represents a lower number of lattice imperfections and defects.[32,33] The GO-based photoanodes show a 33% lower microstrain compared to the pristine hematite photoanodes.

XAFS is an element-specific and bulk local structure-determining probe. Figure 3 displays X-absorption near-edge structure (XANES) spectra and Fourier-transformed spectra of extended X-ray absorption fine structure (EXAFS) functions for Fe K-edges of FTO/$\alpha$-$Fe_2O_3$ and FTO/GO/$\alpha$-$Fe_2O_3$. The XANES spectra for the samples are exactly the same as that of reference $\alpha$-$Fe_2O_3$, where the pre-edge peak denoting a quadrupole transition of 1s → 3d is observed at 7115 eV and the absorption rising feature and energy positions are also the same. EXAFS spectra do not exhibit any significant difference when the samples are compared with the reference $\alpha$-$Fe_2O_3$ in powder. The minor difference is an increase in the intensities of the peaks at 0.8−2.0 and 2.1−3.9 Å. It is due to the enhanced ordering of the nearest Fe−O bond and complicated Fe−Fe and Fe−O bonds, respectively, which is generally observed for the films on substrate. In summary, the graphene oxide layer may not affect in the structure of $\alpha$-$Fe_2O_3$ in an angstrom order. It was further confirmed from the EXAFS analysis that the GO underlayer does not affect the structure of $\alpha$-$Fe_2O_3$ in the angstrom range. With fewer lattice imperfections and defects, we expect higher crystalline photoanodes, which may be a crucial factor for enhanced photocurrent, as reported earlier.[34] The FESEM images of the $\alpha$-$Fe_2O_3$ photoanodes with and without a GO underlayer (Figure 2(a) and (b)) show very similar nanorod morphologies. Thus, the GO underlayer does not affect the growth conditions of the $\alpha$-$Fe_2O_3$ nanorods on FTO substrates. The sintering conditions for the graphene oxide-based samples are crucial factors for the fabrication of devices. Carbon-based samples are highly unstable above 500 °C in an air atmosphere. Sintering them at high temperatures results in a loss of a relatively high amount of carbon as $CO_2$.[18] However, a high sintering temperature (∼800 °C) is required


DOI: 10.1021/acs.jpcc.5b06450
J. Phys. Chem. C 2015, 119, 19996−20002

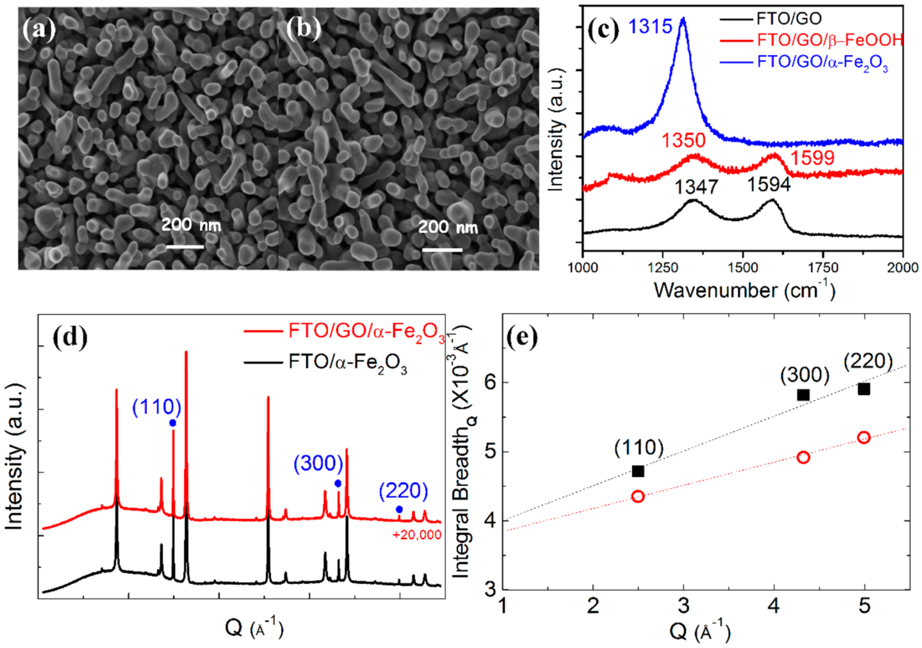


**Figure 2.** FE-SEM images of photoanodes (a) without and (b) with a GO underlayer. (c) Raman spectra of FTO/GO, FTO/GO/$\beta$-FeOOH, and FTO/GO/$\alpha$-$Fe_2O_3$ photoanodes sintered at 800 °C. (d) Synchrotron X-ray diffraction patterns of $\alpha$-$Fe_2O_3$ (marked in blue) photoanodes on FTO substrates (remaining peaks) sintered at 800 °C without (black line) and with a GO (red line) interlayer. (e) Williamson–Hall plots of the hematite peaks denoted as blue dots in (d). The dashed lines represent linear regressions.

**Table 1. Hematite Photoanode Parameters of Crystallite Size ($D$) and Mean Microstrain ($\varepsilon$) Determined from the Williamson–Hall plot from Figure 2(b)[a]**

| | $D$ | $\varepsilon$ | $d$-spacing | $d$-spacing |
|---|---|---|---|---|
| | crystallite size | microstrain | hematite (220) | FTO (400) |
| FTO/$\alpha$-$Fe_2O_3$ | ~169 (20) nm | $5.04\ (1.0) \times 10^{-4}$ | 1.2590 | 1.1907 |
| FTO/GO/$\alpha$-$Fe_2O_3$ | ~169 (05) nm | $3.35\ (0.3) \times 10^{-4}$ | 1.2590 | 1.1913 |
| variation | | 33% ↓ | <0.001% | 0.05% ↑ |

[a]The values in the brackets represent fitting error. Lattice plane distances ($d$) were obtained from the peak position in Figure 2(b).

for the activation of hematite photoanodes.[19] Further information on the changes in GO during activation of hematite was characterized using Raman spectra. Figure 2(c) shows the Raman shift in the range of 1000–2000 $cm^{-1}$, which covers the characteristic bands of graphene-based materials. The FTO/GO samples show two distinct peaks positioned at ~1350 and ~1600 $cm^{-1}$, corresponding to the D- and G-bands, respectively.[35] The presence of GO after hydrothermal synthesis (FTO/GO/$\beta$-FeOOH) was confirmed in the Raman spectra. Sintering at 800 °C for the activation of hematite (FTO/GO/$\alpha$-$Fe_2O_3$) photoanodes decomposes the GO layer into $CO_2$ since carbon-based materials are unstable when sintered above 500 °C under an oxidative atmosphere. The D-band is induced by the local basal plane derivatization and the edge sites that create $sp^3$ distortion, and the G-band arises from the $sp^2$-hybridized graphitic carbon atoms. The Raman spectrum of the FTO/GO/$\beta$-FeOOH photoanode shows the presence of characteristic D- and G-bands, indicating the presence of a GO underlayer after the hydrothermal synthesis. The FESEM images further confirm the presence of GO dispersed on the FTO substrates before hydrothermal synthesis (Figure S4). Figure S5 shows the elemental mapping of C (GO) on the FTO substrates after spin-coating. However, when FTO/GO/$\beta$-FeOOH photoanodes were sintered at a high temperature for activation of the $\alpha$-$Fe_2O_3$ photoanodes, GO in the FTO/GO/$\beta$-FeOOH photoanodes is thermally oxidized, which can be confirmed from the absence of characteristic graphene bands in the Raman spectra of the FTO/GO/$\alpha$-$Fe_2O_3$ photoanodes. The distinct new peak at 1315 $cm^{-1}$ arises from the two phonon scatterings of $\alpha$-$Fe_2O_3$ photoanodes.[36] These results confirm that the GO underlayer acts as a sacrificial layer during the formation of $\alpha$-$Fe_2O_3$ photoanodes. Inhomogeneous GO underlayers cause minimum or no physical damage to the $\alpha$-$Fe_2O_3$ photoanode when sintered at 800 °C (Figures S6 and S7). This resulted in the highest observed photocurrent of 1.3 mA/$cm^2$ at 1.4 V vs RHE, which is 30% higher than the $\alpha$-$Fe_2O_3$ photoanode without a GO underlayer.

The analysis of the FTO/hematite interface will provide additional information to clarify how this GO sacrificial layer enhances the photocurrent. Using electrochemical impedance spectroscopy (EIS), the charge transport kinetics and interfacial properties of the $\alpha$-$Fe_2O_3$ photoanodes with and without a GO underlayer were evaluated. Nyquist plots obtained (Figure 4) from EIS are fitted with an equivalent circuit using ZView, and the following electrochemical parameters are derived from the fitting. $R_S$ is the series resistance, which includes mainly the sheet resistance of the FTO substrates. The parallel $R_{CT1}$ and $CPE_1$ represent the charge transfer resistance and the double-layer capacitance at the FTO/$\alpha$-$Fe_2O_3$ interface, whereas $R_{CT2}$


DOI: 10.1021/acs.jpcc.5b06450
J. Phys. Chem. C 2015, 119, 19996−20002

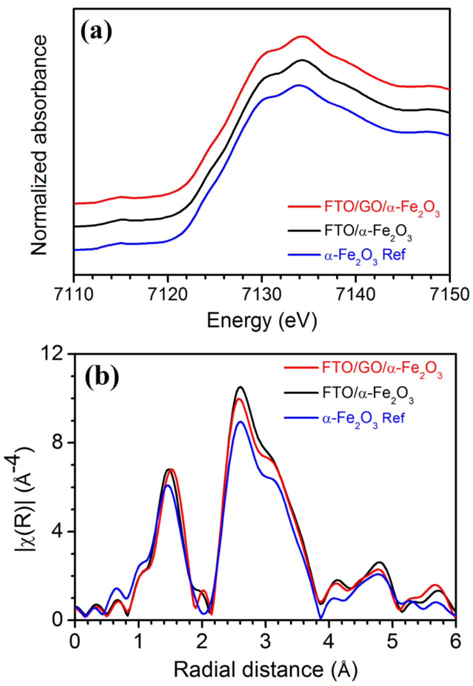


**Figure 3.** (a) XANES spectra and (b) $k^3$-weighted Fourier transforms of EXAFS functions for Fe K-edges of FTO/$\alpha$-$Fe_2O_3$ and FTO/GO/$\alpha$-$Fe_2O_3$. XAFS is an element-specific and bulk local structure-determining probe.

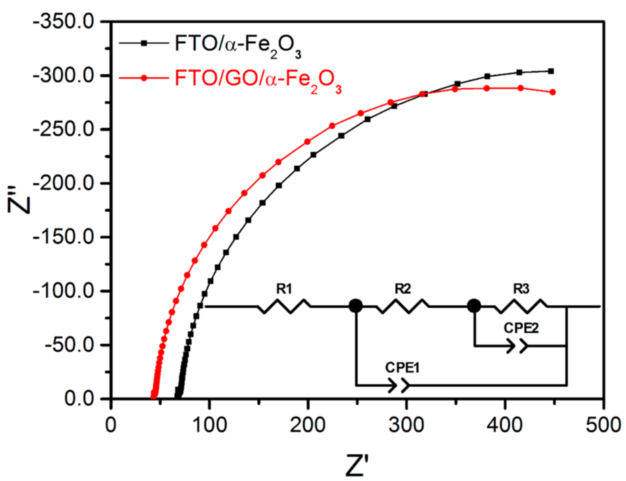


| (R/Ω) (CPE/F) | FTO/ α-$Fe_2O_3$ | FTO/GO/ α-$Fe_2O_3$ | Variation | Remarks |
|---|---|---|---|---|
| $R_S$ | 66.28 | 42.51 | 35% ↓ | **FTO Deformation ↓** |
| $R_{CT1}$ $CPE_1$ | 19.53 $1.98 \times 10^{-5}$ | 13.62 $1.8 \times 10^{-5}$ | 30% ↓ 9% ↓ | **Interface Enhanced** |
| $R_{CT2}$ $CPE_2$ | 680.1 $1.56 \times 10^{-6}$ | 656.2 $1.45 \times 10^{-6}$ | 3% ↓ 7% ↓ | **No change in bulk properties** |

**Figure 4.** Nyquist plots and output of the equivalent circuit model of pristine and FTO/GO/$\alpha$-$Fe_2O_3$ photoanodes sintered at 800 °C using 1 M NaOH under 1 sun standard illumination conditions.

and $CPE_2$, respectively, represent the charge transport resistance of $\alpha$-$Fe_2O_3$ and the double-layer capacitance of the $\alpha$-$Fe_2O_3$/electrolyte interface. From the EIS measurements, the electron transport properties at the FTO/$\alpha$-$Fe_2O_3$ interface can be experimentally deduced.[19,37] For the hematite photoanodes with a GO underlayer, the charge transport resistance across FTO/$\alpha$-$Fe_2O_3$, $R_{CT1}$, was found to decrease from 19 to 13 Ω. The sheet resistance, $R_S$, decreased from 66 to 42 Ω (Figure S8), while the bulk $\alpha$-$Fe_2O_3$ properties remained the same. It is clearly evident from the Nyquist plots obtained for the FTO/GO/$\alpha$-$Fe_2O_3$ photoanodes that the sacrificial GO layer suppresses the electron recombination by facilitating charge transport across the FTO/$\alpha$-$Fe_2O_3$ interface, as GO is a good thermal and electronic conductor. This suggests that the FTO/$\alpha$-$Fe_2O_3$ interface remains enhanced even after the thermal oxidation of GO during activation of the hematite photoanodes. The enhanced FTO/$\alpha$-$Fe_2O_3$ interface was further confirmed by the decrease of the dark current (Figure S9). Such a variation of the dark current may be attributed to improvements of the electron transport properties at the FTO/$\alpha$-$Fe_2O_3$ interface due to an enhanced interface which facilitates the electron transfer from hematite to the FTO conducting substrates,[12,38] which was further confirmed from the incident photon-to-electron conversion efficiency (IPCE) measurements (Figure 5). In comparison to the pristine $\alpha$-$Fe_2O_3$ photoanodes sintered at 800 °C, GO sacrificial layer samples showed uniformly higher IPCE values in the whole visible region. The above results are consistent with the difference of photocurrent densities observed. IPCE is a product of the rate of light-harvesting efficiency ($\eta_{LHE}$), the charge separation efficiency of the photogenerated carriers ($\eta_{SEP}$), and charge injection efficiency ($\eta_{INJ}$)[39]

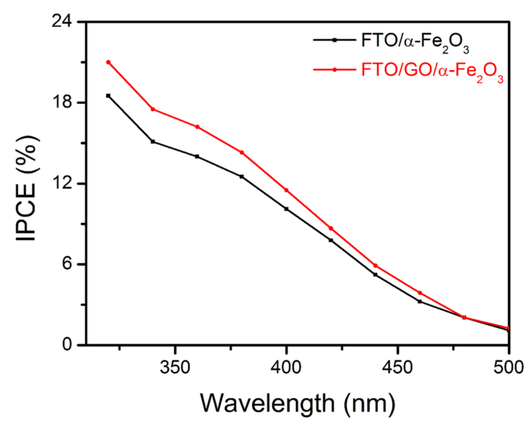


**Figure 5.** Comparison of IPCEs for $\alpha$-$Fe_2O_3$ photoanodes with and without GO-based in FTO substrates sintered at 800 °C, collected at the incident wavelength range from 320 to 500 nm at a potential of 1.23 V vs RHE.

$$\text{IPCE} = \eta_{LHE} \times \eta_{SEP} \times \eta_{INJ} \quad (1)$$

During high-temperature sintering, the effect of the GO sacrificial layer is evident only at the FTO/GO/$\alpha$-$Fe_2O_3$ interface, and this does not affect the $\eta_{LHE}$ and $\eta_{INJ}$ factors as they are dependent on the surface properties more than interfacial properties. Thus, the increase in IPCE can be solely attributed to the enhancement in charge separation efficiency, in other words, to enhanced charge transport kinetics.

Mott−Schottky plots of the hematite photoanodes with and without a GO underlayer are shown in Figure S10 and Table S1. By comparing the slopes of the Mott−Schottky plots, the carrier concentrations calculated for the hematite photoanodes


DOI: 10.1021/acs.jpcc.5b06450
J. Phys. Chem. C 2015, 119, 19996−20002

with and without a GO underlayer were found to be unchanged. Thus, the GO layers only enhance the FTO/$\alpha$-$Fe_2O_3$ interface and do not impact the bulk properties such as the carrier concentration of the hematite photoanodes.

It is well-known that graphene-based materials exhibit extraordinary high thermal conductivities which depends on the number of layers present in a device. With increasing number of layers, the thermal conductivity of graphene-based materials decreases, approaching that of bulk graphite.[40] When sintered at 800 °C for activation of the hematite (FTO/GO/$\alpha$-$Fe_2O_3$) photoanodes, the GO layers before being decomposed act as localized hot zones at the FTO/$\alpha$-$Fe_2O_3$ interface. Thermal oxidation of the GO sacrificial layer may induce a deformation or structural fracture at the FTO/$\alpha$-$Fe_2O_3$ interface at the nanoscale, which is usually caused by residual stress/strain. This residual stress/strain may have a positive impact on the material properties of $\alpha$-$Fe_2O_3$ nanorods during the activation step (800 °C sintering). As the crystallization of $\alpha$-$Fe_2O_3$ from $\beta$-FeOOH occurs, Sn diffusion into the $\alpha$-$Fe_2O_3$ lattice from the FTO substrates and thermal oxidation of GO sacrificial layers takes place at the FTO/GO/$\alpha$-$Fe_2O_3$ interface at the same time. Observing and characterizing the thermal oxidation of the GO sacrificial layer at the FTO/GO/$\alpha$-$Fe_2O_3$ interface at the nanoscale during the activation step is challenging as the other physical properties such as the morphology, bulk crystal structure, carrier concentration, elemental composition (Figure S11), and electron transport resistance remained the same. Localized hot zones formed by the GO underlayer during thermal oxidation play a very crucial role in the reduction of microstrain, as confirmed from the synchrotron X-ray studies. The sacrificial GO underlayer does not affect the structure of $\alpha$-$Fe_2O_3$ in short-range order, as confirmed from the EXAFS analysis. Thus, the effects of GO sacrificial layers are only restricted to the FTO/$\alpha$-$Fe_2O_3$ interface. As a result, the sacrificial GO underlayer may contribute to relaxing inhomogeneous internal strain of $\alpha$-$Fe_2O_3$ nanorods and reduce deformation on the FTO substrate. In other words, reduction of the microstrain minimizes the lattice imperfections and defects at the FTO/$\alpha$-$Fe_2O_3$ interface, which may enhance the charge collection efficiency as demonstrated by the impedance measurements.

## CONCLUSIONS

In summary, a GO layer was prepared by a spin-coating method and used as a sacrificial interlayer between $\alpha$-$Fe_2O_3$ nanostructures and the FTO substrate. We showed that the GO interlayer enhanced the PEC water oxidation performance of $\alpha$-$Fe_2O_3$ photoanodes. This performance enhancement was mainly due to improved interfacial properties (FTO/$\alpha$-$Fe_2O_3$) and minimized lattice imperfections due to the presence of a sacrificial GO underlayer. When $\alpha$-$Fe_2O_3$ photoanodes are sintered at a high temperature for activation, the GO underlayer is thermally oxidized leaving few localized hot zones at the FTO/$\alpha$-$Fe_2O_3$ interface. These localized hot zones play a crucial role in minimizing lattice imperfections in the crystallinity of hematite photoanodes by reducing the microstrain by 33%. The sacrificial GO underlayer not only enhances the charge collection efficiency but also increases the crystallinity with reduced microstrain at the FTO/$\alpha$-$Fe_2O_3$ interface. However, the exact nature of the sacrificial GO interlayers for improved PEC performance still needs further detailed investigation.

## ASSOCIATED CONTENT

### Supporting Information

The Supporting Information is available free of charge on the ACS Publications website at DOI: 10.1021/acs.jpcc.5b06450.

Information on XRD, FE-SEM, EDX, EIS, and XPS of the FTO/$\alpha$-$Fe_2O_3$ and FTO/GO/$\alpha$-$Fe_2O_3$ (PDF)

## AUTHOR INFORMATION


### Corresponding Authors

*Dr. Sun Hee Choi. Tel.: +82-54-279-1552. E-mail: shchoi@postech.ac.kr.

*Prof. Jum Suk Jang. Tel.: +82-63-850-0846. Fax: +82-63-850-0834. E-mail: jangjs75@jbnu.ac.kr.


### Notes

The authors declare no competing financial interest.

## ACKNOWLEDGMENTS

This research was supported by the Basic Science Research Programs through the National Research Foundation of Korea (NRF) funded by the Ministry of Education, Science and Technology (2012R1A6A3A04038530), Korea Ministry of Environment (MOE) as Public Technology Program based on Environmental policy (2014000160001), and the Korea Research Institute of Standards and Science (KRISS) under the project "Establishing Measurement Standards for Inorganic Analysis", grant 15011044.

## REFERENCES


(1) Gratzel, M. Photoelectrochemical Cells. *Nature* **2001**, *414*, 338−344.

(2) Kay, A.; Cesar, I.; Gratzel, M. New Benchmark for Water Photooxidation by Nanostructured $\alpha-Fe_2O_3$ Films. *J. Am. Chem. Soc.* **2006**, *128*, 15714−15721.

(3) Glasscock, J. A.; Barnes, P. R. F.; Plumb, I. C.; Savvides, N. Enhancement of Photoelectrochemical Hydrogen Production from Hematite Thin Films by the Introduction of Ti and Si. *J. Phys. Chem. C* **2007**, *111*, 16477−16488.

(4) Sivula, K.; Zboril, R.; Le Formal, F.; Robert, R.; Weidenkaff, A.; Tucek, J.; Frydrych, J.; Gratzel, M. Photoelectrochemical Water Splitting with Mesoporous Hematite Prepared by a Solution-Based Colloidal Approach. *J. Am. Chem. Soc.* **2010**, *132*, 7436−7444.

(5) Sivula, K.; Le Formal, F.; Gratzel, M. Solar Water Splitting: Progress Using Hematite ($\alpha-Fe_2O_3$) Photoelectrodes. *ChemSusChem* **2011**, *4*, 432−449.

(6) Li, Z. S.; Luo, W. J.; Zhang, M. L.; Feng, J. Y.; Zou, Z. G. Photoelectrochemical Cells for Solar Hydrogen Production: Current State of Promising Photoelectrodes, Methods to Improve their Properties, and Outlook. *Energy Environ. Sci.* **2013**, *6*, 347−370.

(7) Hisatomi, T.; Dotan, H.; Stefik, M.; Sivula, K.; Rothschild, A.; Gratzel, M.; Mathews, N. Enhancement in the Performance of Ultrathin Hematite Photoanode for Water Splitting by an Oxide Underlayer. *Adv. Mater.* **2012**, *24*, 2699−2702.

(8) Bertoluzzi, L.; Ma, S. A. On the Methods of Calculation of the Charge Collection Efficiency of Dye Sensitized Solar Cells. *Phys. Chem. Chem. Phys.* **2013**, *15*, 4283−4285.

(9) Sun, Y. Q.; Chemelewski, W. D.; Berglund, S. P.; Li, C.; He, H. C.; Shi, G. Q.; Mullins, C. B. Antimony-Doped Tin Oxide Nanorods as a Transparent Conducting Electrode for Enhancing Photoelectrochemical Oxidation of Water by Hematite. *ACS Appl. Mater. Interfaces* **2014**, *6*, 5494−5499.

(10) Bassi, P. S.; Gurudayal; Wong, L. H.; Barber, J. Iron Based Photoanodes for Solar Fuel Production. *Phys. Chem. Chem. Phys.* **2014**, *16*, 11834−11842.




DOI: 10.1021/acs.jpcc.5b06450
*J. Phys. Chem. C* 2015, 119, 19996−20002

(11) Le Formal, F.; Gratzel, M.; Sivula, K. Controlling Photoactivity in Ultrathin Hematite Films for Solar Water-Splitting. *Adv. Funct. Mater.* **2010**, *20*, 1099−1107.
(12) Annamalai, A.; Shinde, P. S.; Subramanian, A.; Kim, J. Y.; Kim, J. H.; Choi, S. H.; Lee, J. S.; Jang, J. S. Bifunctional $TiO_2$ Underlayer for $\alpha$−$Fe_2O_3$ Nanorod Based Photoelectrochemical Cells: Enhanced Interface and $Ti^{4+}$ Doping. *J. Mater. Chem. A* **2015**, *3*, 5007−5013.
(13) Hisatomi, T.; Brillet, J.; Cornuz, M.; Le Formal, F.; Tetreault, N.; Sivula, K.; Gratzel, M. A $Ga_2O_3$ Underlayer as an Isomorphic Template for Ultrathin Hematite Films Toward Efficient Photoelectrochemical Water Splitting. *Faraday Discuss.* **2012**, *155*, 223−232.
(14) Wang, D. G.; Zhang, Y. Y.; Wang, J. Q.; Peng, C.; Huang, Q.; Su, S.; Wang, L. H.; Huang, W.; Fan, C. H. Template-Free Synthesis of Hematite Photoanodes with Nanostructured ATO Conductive Underlayer for PEC Water Splitting. *ACS Appl. Mater. Interfaces* **2014**, *6*, 36−40.
(15) Gao, Y.; Yip, H. L.; Hau, S. K.; O'Malley, K. M.; Cho, N. C.; Chen, H. Z.; Jen, A. K. Y. Anode Modification of Inverted Polymer Solar Cells using Graphene Oxide. *Appl. Phys. Lett.* **2010**, *97*, 203306.
(16) Castro Neto, A. H.; Guinea, F.; Peres, N. M. R.; Novoselov, K. S.; Geim, A. K. The electronic properties of graphene. *Rev. Mod. Phys.* **2009**, *81*, 109−162.
(17) Novoselov, K. S.; Falko, V. I.; Colombo, L.; Gellert, P. R.; Schwab, M. G.; Kim, K. A Roadmap for Graphene. *Nature* **2012**, *490*, 192−200.
(18) Zhang, K.; Shi, X.; Kim, J. K.; Lee, J. S.; Park, J. H. Inverse Opal Structured $\alpha$−$Fe_2O_3$ on Graphene Thin Films: Enhanced Photoassisted Water Splitting. *Nanoscale* **2013**, *5*, 1939−1944.
(19) Annamalai, A.; Subramanian, A.; Kang, U.; Park, H.; Choi, S. H.; Jang, J. S. Activation of Hematite Photoanodes for Solar Water Splitting: Effect of FTO Deformation. *J. Phys. Chem. C* **2015**, *119*, 3810−3817.
(20) Kim, J. Y.; Jun, H.; Hong, S. J.; Kim, H. G.; Lee, J. S. Charge Transfer in Iron Oxide Photoanode Modified with Carbon Nanotubes for Photoelectrochemical Water Oxidation: An Electrochemical Impedance Study. *Int. J. Hydrogen Energy* **2011**, *36*, 9462−9468.
(21) Nishanthi, S. T.; Iyyapushpam, S.; Sundarakannan, B.; Subramanian, E.; Padiyan, D. P. Significance of Crystallinity on the Photoelectrochemical and Photocatalytic Activity of $TiO_2$ Nanotube Arrays. *Appl. Surf. Sci.* **2014**, *313*, 449−454.
(22) Rodriguez-Perez, M.; Chacon, C.; Palacios-Gonzalez, E.; Rodriguez-Gattorno, G.; Oskam, G. Photoelectrochemical Water Oxidation at Electrophoretically Deposited $WO_3$ Films as a Function of Crystal Structure and Morphology. *Electrochim. Acta* **2014**, *140*, 320−331.
(23) Hummers, W. S.; Offeman, R. E. Preparation of Graphitic Oxide. *J. Am. Chem. Soc.* **1958**, *80*, 1339−1339.
(24) Kovtyukhova, N. I.; Ollivier, P. J.; Martin, B. R.; Mallouk, T. E.; Chizhik, S. A.; Buzaneva, E. V.; Gorchinskiy, A. D. Layer-by-Layer Assembly of Ultrathin Composite Films from Micron-Sized Graphite Oxide Sheets and Polycations. *Chem. Mater.* **1999**, *11*, 771−778.
(25) Kannan, A. G.; Zhao, J.; Jo, S. G.; Kang, Y. S.; Kim, D.-W. Nitrogen and Sulfur Co-doped Graphene Counter Electrodes with Synergistically Enhanced Performance for Dye-Sensitized Solar Cells. *J. Mater. Chem. A* **2014**, *2*, 12232−12239.
(26) Vayssieres, L.; Beermann, N.; Lindquist, S. E.; Hagfeldt, A. Controlled Aqueous Chemical Growth of Oriented Three-Dimensional Crystalline Nanorod Arrays: Application to Iron(III) Oxides. *Chem. Mater.* **2001**, *13*, 233−235.
(27) Ling, Y. C.; Wang, G. M.; Wheeler, D. A.; Zhang, J. Z.; Li, Y. Sn-Doped Hematite Nanostructures for Photoelectrochemical Water Splitting. *Nano Lett.* **2011**, *11*, 2119−2125.
(28) Ravel, B.; Newville, M. ATHENA, ARTEMIS, HEPHAESTUS: Data Analysis for X-ray Absorption Spectroscopy using IFEFFIT. *J. Synchrotron Radiat.* **2005**, *12*, 537−541.
(29) Yoon, K. Y.; Lee, J. S.; Kim, K.; Bak, C. H.; Kim, S. I.; Kim, J. B.; Jang, J. H. Hematite-Based Photoelectrochemical Water Splitting Supported by Inverse Opal Structures of Graphene. *ACS Appl. Mater. Interfaces* **2014**, *6*, 22634−22639.
(30) Williamson, G. K.; Hall, W. H. X-Ray Line Broadening from Filed Aluminium and Wolfram. *Acta Metall.* **1953**, *1*, 22−31.
(31) Oehzelt, M.; Resel, R.; Suess, C.; Friedlein, R.; Salaneck, W. R. Crystallographic and Morphological Characterization of Thin Pentacene Films on Polycrystalline Copper Surfaces. *J. Chem. Phys.* **2006**, *124*, 054711.
(32) Dom, R.; Baby, L. R.; Kim, H. G.; Borse, P. H. Enhanced Solar Photoelectrochemical Conversion Efficiency of ZnO:Cu Electrodes for Water-Splitting Application. *Int. J. Photoenergy* **2013**, *2013*, 1−9.
(33) Pawar, N. B.; Mali, S. S.; Kharade, S. D.; Gang, M. G.; Patil, P. S.; Kim, J. H.; Hong, C. K.; Bhosale, P. N. Influence of Vacuum Annealing on the Structural and Photoelectrochemical Properties of Nanocrystalline $MoBi_2S_5$ Thin Films. *Curr. Appl. Phys.* **2014**, *14*, 508−515.
(34) Kondalkar, V. V.; Mali, S. S.; Pawar, N. B.; Mane, R. M.; Choudhury, S.; Hong, C. K.; Patil, P. S.; Patil, S. R.; Bhosale, P. N.; Kim, J. H. Microwave-Assisted Rapid Synthesis of Highly Porous $TiO_2$ Thin Films with Nanocrystalline Framework for Efficient Photoelectrochemical Conversion. *Electrochim. Acta* **2014**, *143*, 89−97.
(35) Jeon, Y. J.; Yun, J. M.; Kim, D. Y.; Na, S. I.; Kim, S. S. Moderately Reduced Graphene Oxide as Hole Transport Layer in Polymer Solar Cells via Thermal Assisted Spray Process. *Appl. Surf. Sci.* **2014**, *296*, 140−146.
(36) Lubbe, M.; Gigler, A. M.; Stark, R. W.; Moritz, W. Identification of Iron Oxide Phases in Thin Films Grown on $Al_2O_3$(0001) by Raman Spectroscopy and X-ray Diffraction. *Surf. Sci.* **2010**, *604*, 679−685.
(37) Lopes, T.; Andrade, L.; Ribeiro, H. A.; Mendes, A. Characterization of Photoelectrochemical Cells for Water Splitting by Electrochemical Impedance Spectroscopy. *Int. J. Hydrogen Energy* **2010**, *35*, 11601−11608.
(38) Shi, X. J.; Zhang, K.; Park, J. H. Understanding the Positive Effects of (Co-Pi) Co-catalyst Modification in Inverse-Opal Structured $\alpha$−$Fe_2O_3$-based Photoelectrochemical Cells. *Int. J. Hydrogen Energy* **2013**, *38*, 12725−12732.
(39) Tamirat, A. G.; Su, W. N.; Dubale, A. A.; Chen, H. M.; Hwang, B. J. Photoelectrochemical water splitting at low applied potential using a NiOOH coated codoped (Sn, Zr) $\alpha$−$Fe_2O_3$ photoanode. *J. Mater. Chem. A* **2015**, *3*, 5949−5961.
(40) Balandin, A. A. Thermal Properties of Graphene and Nanostructured Carbon Materials. *Nat. Mater.* **2011**, *10*, 569−581.



DOI: 10.1021/acs.jpcc.5b06450
J. Phys. Chem. C 2015, 119, 19996−20002